



1 Validation of formaldehyde products from three satellite retrievals 2 (OMI SAO, OMPS-NPP SAO, and OMI BIRA) in the marine 3 atmosphere with four seasons of ATom aircraft observations

4 Jin Liao^{1,2}, Glenn M. Wolfe¹, Alex E. Kotsakis^{1,2,*}, Julie M. Nicely^{1,3}, Jason M. St. Clair^{1,2}, Thomas F.
5 Hanisco¹, Gonzalo González Abad⁴, Caroline R. Nowlan⁵, Zolal Ayazpour^{5,6}, Isabelle De Smedt⁷, Eric
6 C. Apel⁸, Rebecca S. Hornbrook⁸

7 ¹Atmospheric Chemistry and Dynamic Laboratory, NASA Goddard Space Flight Center, Greenbelt, MD, USA

8 ²Goddard Earth Sciences Technology and Research (GESTAR II), University of Maryland, Baltimore County, MD, USA

9 ³Earth Resources Technology (ERT) Inc., Laurel, MD, USA

10 ⁴Earth System Science Interdisciplinary Center (ESSIC), University of Maryland, College Park, MD, USA

11 ⁵Center for Astrophysics Harvard-Smithsonian, Cambridge, MA, USA

12 ⁶Department of Civil, Structural and Environmental Engineering, University of Buffalo, Buffalo, NY, USA

13 ⁷Royal Belgian Institute for Space Aeronomy (BIRA-IASB), Brussels, Belgium

14 ⁸Atmospheric Chemistry Observations & Modeling Laboratory, National Center for Atmospheric Research (NCAR), Boulder,
15 CO, USA

16 *Now at Earth System Science Interdisciplinary Center (ESSIC), University of Maryland, College Park, MD, USA

17

18 *Correspondence to:* Jin Liao (jin.liao@nasa.gov)

19

20 **Abstract.** Formaldehyde (HCHO) in the atmosphere is an intermediate product from the oxidation of methane and non-
21 methane volatile organic compounds. In remote marine regions, HCHO variability is closely related to atmospheric
22 oxidation capacity and modeled HCHO in these regions is usually added as a global satellite HCHO background. Thus, it is
23 important to understand and validate the levels of satellite HCHO over the remote oceans. Here we intercompare three
24 satellite retrievals of total HCHO columns (OMI-SAO (v004), OMPS-NPP SAO, and OMI BIRA) and validate them against
25 in situ observations from the NASA Atmospheric Tomography Mission (ATom) mission. All retrievals are correlated with
26 ATom integrated columns over remote oceans, with OMI SAO (v004) showing the best agreement. Three satellite HCHO
27 retrievals and in situ ATom columns all generally captured the spatial and seasonal distributions of HCHO in the remote
28 ocean atmosphere. Retrieval bias varies by latitude and season, but a persistent low bias is found in all products at high
29 latitudes and the general low bias is most severe for the OMI BIRA product. Examination of retrieval components reveals
30 slant column corrections have a larger impact on the retrievals over remote marine regions while AMFs play a smaller role.
31 This study informs that the potential latitude-dependent biases in the retrievals require further investigation for improvement
32 and should be considered when using marine HCHO satellite data, and vertical profiles from in situ instruments are crucial
33 for validating satellite retrievals.

34

35



36 1 Introduction

37 Formaldehyde (HCHO) in the marine atmosphere is mainly produced from oxidation of methane. Non-methane volatile
38 organic compounds (VOCs) transported from continents and potentially VOCs emitted at the ocean surface (Guenther et al.,
39 1995; Novak and Bertram, 2020) may also contribute to the marine HCHO. Methane is the dominant precursor of HCHO in
40 the remote atmosphere and oxidation of methane by hydroxyl radical (OH) represents ~ 80% of the global HCHO source
41 (Fortems-Cheiney et al., 2012; Wolfe et al., 2019). Satellite HCHO columns have been used to estimate the levels of
42 atmospheric oxidant OH, which plays an important role in removing air pollutants and greenhouse gas methane (Wolfe et al.,
43 2019). HCHO in the clean remote ocean atmosphere is considered as HCHO tropospheric background due to the short
44 atmospheric lifetime of HCHO of a few hours and its source locations. The column abundance of HCHO ranges from
45 $\sim 1 \times 10^{15}$ molec cm^{-2} in the remote troposphere (Vigouroux et al., 2018; Zhu et al., 2020) to the order of 10^{16} molec cm^{-2} over
46 continental regions (Zhu et al., 2016).

47

48 HCHO is one of the few VOCs that can be observed from space. Satellite HCHO observations have been obtained by Global
49 Ozone Monitoring Experiment (GOME) (1995-2011) (Chance et al., 2000; Thomas et al., 1998), the Scanning Imaging
50 Absorption SpectroMeter for Atmospheric ChartographY (SCIAMACHY) (2002-2012) (De Smedt et al., 2008), GOME-2
51 (2006-2021/2012-present/2018-present) (De Smedt et al., 2012), the Ozone Monitoring Instrument (OMI) (2004-present)
52 (De Smedt et al., 2015; González Abad et al., 2015), the Ozone Mapping and Profiler Suite (OMPS) on Suomi NPP (Li et
53 al., 2015; González Abad et al., 2016; Nowlan et al., 2023) and on NOAA-20 (2017-present) (Nowlan et al., 2023), and the
54 TROPOspheric Monitoring Instrument (Sentinel-5P/TROPOMI) (2017-present) (De Smedt et al., 2021, 2018).
55 Geostationary satellite instruments also retrieve HCHO, including the Geostationary Environment Monitoring Spectrometer
56 (GEMS) (Kim et al., 2020; Kwon et al., 2019) over East Asia (2020-present), Tropospheric Emissions: Monitoring of
57 Pollution (TEMPO) (Chance et al., 2019) over North America (2023-present) and the upcoming European Sentinel-4
58 mission (Gulde et al., 2017). Major retrieval algorithms for HCHO include those developed by the Smithsonian
59 Astrophysical Observatory (SAO), Belgian Institute for Space Aeronomy (BIRA), and NASA Goddard Space Flight Center
60 (GSFC). These algorithms have evolved over time.

61

62 Previous studies have validated satellite HCHO retrievals with airborne and ground-based in situ and remote sensing
63 instruments in different settings and contexts. Zhu et al. (2016) indirectly evaluated six retrievals from four sensors against
64 airborne observations in the isoprene-rich Southeast U.S. using a model as an intermediary, finding a low bias in the mean
65 by 20-51% for all retrievals. Zhu et al. (2020) extend this method to indirectly validate OMI SAO v003 data with in-situ
66 HCHO measurements from 12 aircraft campaigns over North America, East Asia, and the remote Pacific Ocean. They found
67 that the OMI SAO v003 product has negative biases (-44:5% to -21:7%) under high-HCHO conditions and high biases
68 (+66:1% to +112:1 %) under low-HCHO conditions (Zhu et al., 2020). De Smedt et al. (2021) validated TROPOMI and



69 OMI-BIRA HCHO against a Multi-axis differential optical absorption spectroscopy (MAX-DOAS) ground network, finding
70 that compared to the MAX-DOAS ground network, TROPOMI HCHO columns are biased low especially for high
71 concentrations and OMI-BIRA HCHO columns are biased high at low concentrations and biased low at high concentrations
72 (De Smedt et al., 2021). In validation using Fourier transform infrared (FTIR) data, TROPOMI HCHO columns were biased
73 high for low concentrations sites and biased low for high concentrations sites and the correlation between TROPOMI and
74 FTIR HCHO columns yields a slope of 0.64 and an intercept of 1.10×10^{15} molecules cm^{-2} (Vigouroux et al., 2020). OMPS
75 Suomi NPP and NOAA-20 HCHO columns generally have good agreement with NDACC FTIR observations at 24 sites. The
76 linear regression between OMPS-NPP and FTIR HCHO columns yields a slope of 0.82 and an intercept of 5.71×10^{14}
77 molecules cm^{-2} and the linear regression between OMPS-NOAA20 and FTIR reveals a slope of 0.92 and an intercept of 6.76
78 $\times 10^{14}$ molecules cm^{-2} (Kwon et al., 2023). OMPS-NPP and OMPS-NOAA20 HCHO columns are also biased high
79 compared to FTIR measurements for sites with low HCHO levels (Kwon et al., 2023).

80

81 Most validation efforts focus on continental regions, while comparatively few examine the remote marine atmosphere. No
82 previous validation of satellite HCHO over the remote oceans with airborne in situ measurement was performed before the
83 NASA ATom field campaigns (2016–2018). OMI SAO v003 retrieval has been compared to two seasons of ATom
84 observations over both Pacific and Atlantic Oceans (Wolfe et al., 2019) and over the clean Pacific Ocean (Zhu et al., 2020),
85 with HCHO columns ranging from 1×10^{15} to 8×10^{15} molecules cm^{-2} . The ground FTIR HCHO measurements at Mauna
86 Loa in the Pacific Ocean domain are about 1×10^{15} molecules cm^{-2} for the background atmosphere measurements
87 (Vigouroux et al., 2018).

88

89 The accuracy of model predicted HCHO over the Pacific Ocean affects the global HCHO background in satellite retrievals.
90 In satellite HCHO retrievals, differential HCHO slant columns are often derived using spectra measured over a reference
91 sector in the Pacific Ocean, and modeled HCHO columns over the reference sector are added back to account for the real
92 HCHO levels over the reference sector (De Smedt et al., 2018; Nowlan et al., 2023). The locations of the area in the Pacific
93 Ocean used as reference sectors vary among different retrievals (De Smedt et al., 2018; Nowlan et al., 2023). Modeled
94 HCHO levels over the remote Pacific Ocean also play a role in correcting some biases such as latitude-dependent biases in
95 slant columns (De Smedt et al., 2018; Nowlan et al., 2023). Consequently, validating satellite HCHO over the remote ocean
96 would aid in assessing the satellite's ability to capture background HCHO levels accurately and enhancing our understanding
97 of these baseline levels.

98

99 Here we present a systematic comparison of in situ HCHO columns from four seasons of ATom observations with three
100 commonly-used satellite retrievals. Study objectives include 1) quantify spatial and seasonal retrieval bias, 2) quantify
101 differences between retrievals, and 3) identify relative contributions of retrieval components to inter-retrieval differences and
102 overall bias.



103

104 2. Methods

105 2.1 ATom observations

106 The NASA ATom mission studied atmospheric composition from near pole-to-pole over the Pacific and Atlantic remote
107 oceans with frequent vertical profiling from above the sea surface (100 m) to 10-12 km altitude for four seasons during
108 2016-2018 (Thompson et al., 2022).

109

110 The primary source of in situ HCHO measurements for this study is the In Situ Airborne Formaldehyde (ISAF) instrument
111 (Cazorla et al., 2015). ISAF data are reported at 1 Hz with a 1σ precision of 30 pptv. Systematic uncertainty is estimated as
112 $10\% + 10$ pptv based on pre- and post-mission calibration against compressed gas standards. ISAF measurements are not
113 available during the second half of ATom 4, thus we also use HCHO observations from the Trace Organic Gas Analyzer
114 (TOGA) instrument (Apel et al., 2003, 2015). The TOGA reporting period is 2 minutes, and reported HCHO accuracy is
115 $40\% \pm 40$ pptv. Brune et al. (2020) performed a comparison of ISAF and TOGA data for all four ATom deployments and
116 found mission-to-mission variability in measurement agreement, with relatively good agreement for ATom-4. Similarly, we
117 find that the two measurements agree well for this deployment (Figure S1, slope of 1.1). Due to the higher accuracy and
118 measurement frequency of ISAF than TOGA, ISAF HCHO measurements from ATom are used when available.

119

120 ATom in situ HCHO composite columns are derived from the ATom vertical profiles. Ascents and descents occur along
121 transits between locations and typically cover 200-450 km in horizontal distance (Wolfe et al., 2019). In situ HCHO
122 columns are calculated using the method described in Wolfe et al. (2019). Each profile is averaged to an altitude grid of 0 to
123 10 km with 200 m spacing. Few measurements above 10 km are excluded. The lowest (or highest) altitude measurements are
124 extrapolated to the surface 0 km or (10 km) using the average of the two lowest (or highest) altitude measurements of that
125 profile. Missing data in between are linearly interpolated. Columns are filtered to include only profiles with solar zenith
126 angle smaller than 80° , minimum altitude ≤ 600 m, maximum altitude ≥ 8 km, fraction of interpolated grids < 0.2 , and
127 fraction of extrapolation data < 0.25 . Average gas profiles from OMI SAO HCHO retrievals are used to estimate the
128 contribution of HCHO above 10 km to the total HCHO column. The calculated fraction of HCHO above 10 km (relative to
129 the total column) is 0.045 ± 0.002 . This value is used to scale up in situ HCHO columns for comparison with satellite
130 retrievals.

131



132 2.2 Satellite HCHO retrieval products

133 2.2.1 OMI SAO (v004)

134 OMI was launched in 2004 onboard the NASA Aura satellite. It has a native spatial resolution at nadir of $24 \times 13 \text{ km}^2$ (Table
135 1) with daily global coverage at a local overpass time of 13:30. The Smithsonian Astrophysical Observatory (SAO) version
136 004 retrieval is the updated version of OMI SAO v003 (González Abad et al., 2015) and is identical to the OMPS-NPP SAO
137 retrieval (Nowlan et al., 2023). The algorithm involves two main steps: 1) Following line shape and spectral calibration,
138 spectral fitting at 328.5-356.5 nm range for individual ground pixel is applied and a reference spectrum from a clean region
139 over the Pacific Ocean is used with the measured spectrum to derive the differential slant column (ΔSCD), and 2) converting
140 the resultant ΔSCD to vertical column density (VCD) using slant column corrections and the air mass factor (AMF). The
141 HCHO absorption cross section used in OMI SAO 004 is from Chance and Orphal (2011) at 300 K (Table 1). The location
142 of the reference spectrum is over the clean Pacific Ocean but varies slightly day-to-day due to orbit overpass location. The
143 OMI SAO reference spectrum at each across-track position is determined by averaging all spectra collected at that position
144 between latitudes 30° S and 30° N from the orbit closest in time and with an equatorial crossing closest to 160° W and within
145 140° W and 180° W (Nowlan et al., 2023). The spectra at the reference locations are also used for slant column reference
146 sector corrections including HCHO background addition as described below.

147

148 The ΔSCD is converted to VCD through Eq. (1).

149

$$150 \text{VCD} = (\Delta\text{SCD} + \text{SCD}_{\text{Ref}} + \text{SCD}_{\text{B}})/\text{AMF}, \quad (1)$$

151

152 Where SCD_{Ref} is reference sector correction; SCD_{B} is bias correction; and $\Delta\text{SCD} + \text{SCD}_{\text{Ref}} + \text{SCD}_{\text{B}}$ is also referred to as the
153 corrected slant column. The SCD_{Ref} corrects the cross-track pixel dependence sensitivity and adds HCHO background slant
154 columns from the reference region from a chemical transport model (VCD from CTM model \times AMF) (Nowlan et al., 2023).
155 The SCD_{B} is from the modeled columns of HCHO and used to correct what are primarily latitude-dependent biases in the
156 retrieved ΔSCD , likely due to interfering absorbers and insufficiently corrected instrument calibration issues (Nowlan et al.,
157 2023).

158

159 The AMF defines the mean photon path across the atmosphere and is used in the retrievals to convert slant columns into
160 vertical columns (Eq. (1)). AMF is calculated by the product of altitude-dependent gas phase HCHO shape factors (S) and
161 scattering weights (w) integrated along the vertical coordinate (Eq. (2)). Shape factor (S) is the normalized HCHO vertical
162 number density and calculated from the product of altitude dependent HCHO mixing ratio C and air mass density M
163 normalized by HCHO column density (see Eq. (3)). The HCHO vertical mixing ratio profile (or *a priori* profile) comes from
164 a GEOS-Chem 2018 monthly climatology at $0.5^\circ \times 0.5^\circ$ resolution. Scattering weights are altitude-dependent HCHO



165 measurement sensitivities and are calculated from a vector multiple-scatter multilayer discrete-ordinate radiative transfer
166 model (VLIDORT) v2.8 (Spurr, 2006). Scattering weights depend on the viewing angles, surface albedo, surface pressure
167 and clouds. The scattering and absorption of abnormal aerosol loading can also affect scattering weights and may not be
168 properly represented in calculated scattering weights (e.g., unpredicted biomass burning plumes).

$$169 \quad \text{AMF} = \int_0^z w(z)S(z)dz, \quad (2)$$

$$170 \quad S(z) = \frac{c(z)M(z)}{\int_0^z c(z)M(z)dz}, \quad (3)$$

171

172 Previous comparisons of airborne to satellite HCHO data used OMI SAO v003 (Wolfe et al., 2019; Zhu et al., 2020). OMI
173 SAO v003 retrieves slant column density using direct differential optical absorption spectroscopy (DOAS) (Gonzalez Aabd et
174 al., 2015). To show the difference between OMI SAO v004 and OMI SAO v003, the global maps of HCHO from OMI SAO
175 v004, OMI SAO v003 and their difference with the temporal average for the ATom-1 time period are provided in supplementary
176 Figure S2.

177 **2.2.2 OMPS-NPP SAO**

178 OMPS is onboard the joint NASA/NOAA Suomi National Polar-orbiting Partnership (NPP) satellite that was launched in 2011
179 with a spatial resolution at nadir of 50×50 km and daily global coverage. OMPS also has an equatorial crossing time of about
180 13:30 local time. The retrieval of OMPS-SAO is described in Nowlan et al., (2023), and is identical to that described above
181 (Sect. 2.1.1). The spatial and temporal coverage of OMPS and OMI differ due to both their native spatial resolutions and the
182 OMI row anomaly (González Abad et al., 2016).

183 **2.2.3. OMI BIRA**

184 OMI BIRA is the European Union Quality Assurance for Essential Climate Variables (QA4ECV) product (De Smedt et al.,
185 2015; Zara et al., 2018). It is basically the same retrieval algorithm as the operational product of TROPOspheric Monitoring
186 Instrument (TROPOMI) launched in October 2017 (De Smedt et al., 2021). The detailed retrieval algorithms are described in
187 De Smedt et al. (2018) and only a brief description is provided here. OMI BIRA retrieval also involves two steps. The
188 spectra fitting window is 328.5–359 nm, slightly larger than SAO retrievals.

189 For OMI BIRA, slant column densities are converted to vertical columns as Eq. (5).

$$190 \quad \text{VCD} = (\Delta\text{SCD} - N_{s,0})/\text{AMF} + N_{v,0}, \quad (5)$$

191 $N_{s,0}$, the slant column correction, corrects the remaining global offset and possible stripes (cross-track pixel dependence
192 sensitivity) of the differential slant column. $N_{v,0}$, the vertical column correction, is from the TM5 model to compensate for a
193 background HCHO level due to methane oxidation in the equatorial Pacific (De Smedt et al., 2021). The corrected slant column
194 is defined as differential slant column (ΔSCD) minus slant column correction ($N_{s,0}$) plus the product of vertical column



195 correction ($N_{v,0}$) and AMF. The OMI BIRA gas profile comes from TM5-MP model $1^\circ \times 1^\circ$ daily data. The radiative transfer
 196 model for OMI BIRA is VLIDORT v2.7 (De Smedt et al., 2017), a slightly different version from that used in the SAO
 197 retrievals. In the OMI BIRA retrieval, the location of reference sector for destripping and global offset correction is between
 198 latitudes 5°S and 5°N and longitudes 120°W and 180°W and for zonal correction is between latitudes 90°S and 90°N and
 199 longitudes 120°W and 180°W (De Smedt et al., 2017). Considering the locations of the reference sectors (see Figure S3),
 200 understanding of the HCHO concentration over the clean Pacific Ocean is important for evaluating the accuracy of satellite
 201 HCHO retrievals.

202

203 Table 1. Parameters in satellite retrievals

	Nadir pixel resolution (km ²)	Fitting windows (nm)	HCHO absorption cross section	Chemical Transport Model (CTM)	Radiative transfer model and wavelength for calculation	Trace gas profiles	Reference sector locations
OMI SAO	24×13	328.5-356.5	HITRAN (Chance and Orphal, 2011), 300 K	GEOS-Chem v09-01-03	VLIDORT v2.8, 340 nm	GEOS-Chem 2018 monthly climatology $0.5^\circ \times 0.5^\circ$	Latitudes: $30^\circ\text{S} - 30^\circ\text{N}$ longitudes: an equatorial crossing closest to 160°W and between 140°W and 180°W
OMPS-NPP SAO	50×50	the same as above	the same as above	the same as above	the same as above	the same as above	the same as above
OMI BIRA	24×13	328.5-359	Meller and Moortgat, 2000, 298K	TM5-MP	VLIDORT v2.7, 340 nm	TM5-MP daily profiles, $1^\circ \times 1^\circ$	Destripping and global offset correction: latitudes $5^\circ\text{S} - 5^\circ\text{N}$, longitudes $120^\circ\text{W} - 180^\circ\text{W}$; Zonal correction: latitudes $90^\circ\text{S} - 90^\circ\text{N}$, longitudes $120^\circ\text{W} - 180^\circ\text{W}$

204

205 2.2.4 Retrieval uncertainties

206 Uncertainties in satellite retrievals come from instrument calibrations, slant column fitting processes, slant column
 207 corrections, and AMF calculations. Averaging damps random uncertainties, while the systematic uncertainties remain
 208 (Nowlan et al., 2023). Instrument noise, choice of fitting windows, HCHO cross-section error, surface reflectance, *a priori*
 209 profiles, vertical distribution and properties of clouds and aerosols all can contribute to the overall systematic uncertainties of
 210 satellite HCHO products. In the OMPS SAO retrieval, the systematic uncertainty in corrected slant column is about 20%
 211 (Nowlan et al., 2023). The error from surface reflectance is about 5% over water, from aerosols is about 0.3% in global mean
 212 (but considerably larger in polluted regions and individual observations), from profile shape is 5% at low HCHO
 213 concentrations, from cloud fraction is 1% and from cloud pressure is 5-15% (Nowlan et al., 2023). The total systematic error
 214 is about 26%. We assume other retrievals have similar or smaller systematic errors, as OMPS SAO uses climatological cloud
 215 pressure and probably has the largest uncertainty (Nowlan et al., 2023).

216

217 2.2.5 Satellite data filtering and gridding

218 OMI SAO and OMPS SAO HCHO data use the same categories to filter the data while OMI BIRA use slightly different
 219 filtering categories. SAO L2 data with solar zenith angle $> 60^\circ$, cloud fraction $> 40\%$, main data quality flag not equal to 0



220 are excluded. OMI BIRA L2 data with solar zenith angle $> 60^\circ$, cloud fraction $> 40\%$, and processing error flag $\neq 0$ but \leq
221 255 are excluded.

222

223 The 3-D data such as gas profiles are first re-gridded to a universal vertical grid coordinate for all pixels. The L2 2-D and 3-
224 D data are then gridded into $0.5^\circ \times 0.5^\circ$ using an area weighted average (e.g. AMF, Gas Profiles), shown in Eq. (6), or
225 uncertainty weighted average (e.g., HCHO column density), as shown in Eq. (7).

226

$$227 \quad \overline{C_{ai}} = \frac{\sum_n C_n A_{n,i}}{\sum_n A_{n,i}}, \quad (6)$$

$$228 \quad \overline{C_i} = \frac{\sum_n \frac{C_n A_{n,i}}{A_n E_n^2}}{\sum_n \frac{A_{n,i}}{A_n E_n^2}}, \quad (7)$$

229 where $\overline{C_{ai}}$ is the area weighted average value (such as AMF) for grid i , $\overline{C_i}$ is the uncertainty weighted average value (such
230 as HCHO column density) for grid i , C_n is the HCHO column density for pixel n , $A_{n,i}$ is the area contribution of pixel n to
231 grid i , A_n is the total area of pixel n , and E_n is the uncertainty of HCHO column density for pixel n .

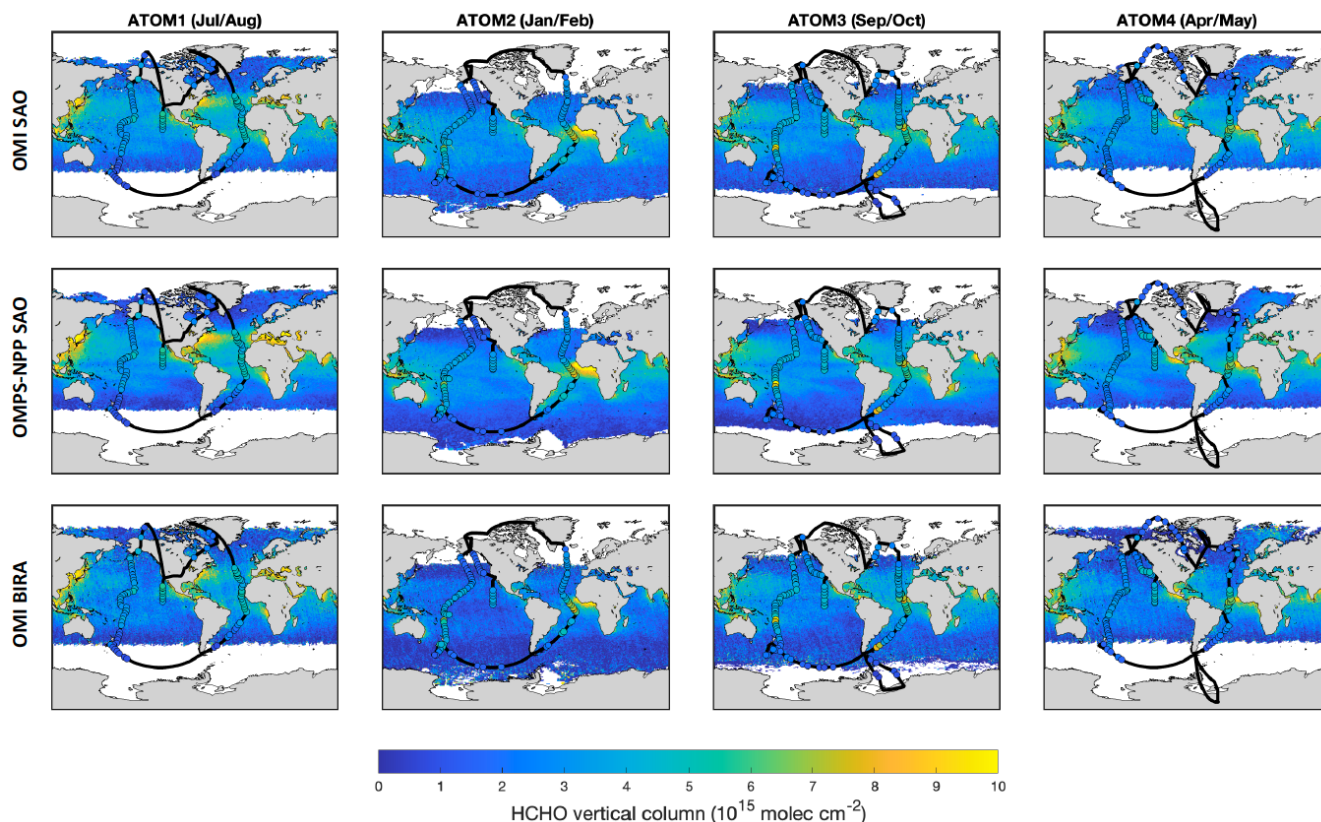
232

233 The gridded $0.5^\circ \times 0.5^\circ$ daily satellite HCHO data are averaged over each ATom period (ATom-1: 29 July – 23 August,
234 2016; ATom-2: 26 January – 21 February, 2017; ATom-3: 28 September – 27 October, 2017; ATom-4: 24 April – 21 May,
235 2018). Differential slant column, slant column corrected, and vertical column all use uncertainty weighted averaging (Eq.
236 (6)). For comparison to in situ HCHO composite columns, the latitude and longitude coverage of the in situ profile are
237 identified and the satellite HCHO grids intercepted with the profile latitudes and longitudes are averaged to compare to the
238 calculated in situ HCHO composite column.

239 3. Results and discussions

240 3.1 Global distribution and seasonal variability of HCHO in the marine atmosphere

241 Global HCHO distributions from all three retrievals and in situ composite columns across the Pacific and Atlantic Oceans
242 show enhancement in the tropics and decrease toward polar regions (Figures 1 and 2). The HCHO vertical column density
243 over the remote ocean atmosphere ranges from about 4×10^{15} molecules cm^{-3} at low latitudes to about 1×10^{15} molecules cm^{-3}
244 at high latitudes. These large-scale features reflect similar latitudinal and seasonal variability in OH and photolysis rates.
245 Although the random noise for satellite HCHO such as OMPS SAO is about 3.5×10^{15} molecules cm^{-3} (Nowlan et al., 2023),
246 averaging in time and space largely reduces the noise and thus the variability of HCHO in the remote ocean atmosphere can
247 be well captured with near one-month average data. In situ HCHO columns corroborate the latitudinal-dependent HCHO
248 trend over the remote oceans.



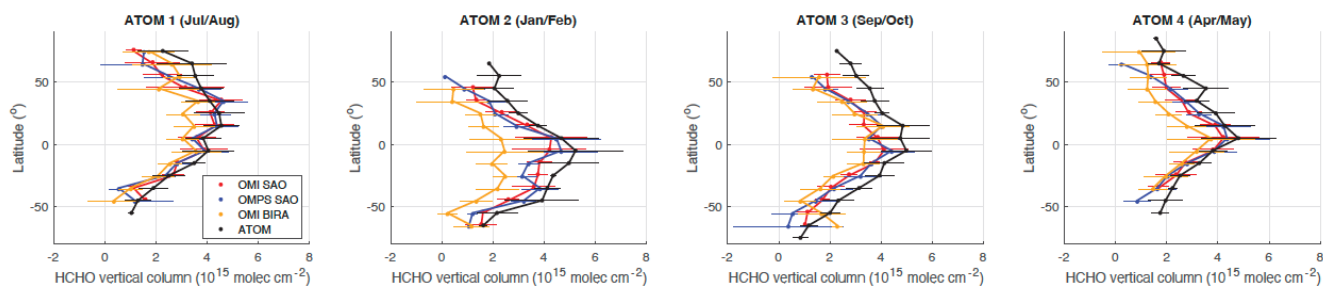
249
250 **Figure 1. Maps of HCHO vertical column density from three satellite retrievals (OMI-SAO, OMPS-SAO and OMI-BIRA, top to**
251 **bottom) over the oceans during four ATom measurement seasons (left to right) overlaid with in situ HCHO columns (colored dots)**
252 **along the ATom flight tracks (black lines). The color bar for both satellite and in situ HCHO composite columns is the same and**
253 **saturates at both ends.**

254
255 Besides background methane oxidation, continental outflow also affects marine HCHO. All three satellite retrievals capture
256 the continental outflow of HCHO or its precursors from East Asia, North America, Africa, and South Asia (Figure 1). These
257 enhancements can be significant; for example, HCHO off the Atlantic coast of equatorial Africa in February reaches $1.1 \times$
258 10^{16} molecules cm^{-2} , sampled by ATom-2. ATom-3 observed enhanced HCHO in the vicinity of Fiji island when DC8
259 landed and took off (Figure 1). This enhancement is likely due to local emissions and thus is excluded from the analysis
260 below. Enhanced HCHO mixing ratios near Argentina is also observed during ATom-3. This may be due to a transient
261 biomass burning plume, as black carbon is also enhanced at this time, though carbon monoxide (CO) is not enhanced.
262 Satellite HCHO data also do not show a sustained enhancement at this location. The in situ HCHO composite column
263 enhancement in ATom-3 near Argentina was also excluded from the following analysis.

264
265 Zonal mean HCHO varies with season (Figure 2). During ATom-1 in July and August (boreal summer), peak HCHO occurs
266 in a broad band between latitudes near $15\text{--}35^\circ\text{N}$. During ATom 2 in January and February (austral summer), the maximum
267 HCHO latitude occurs near 5°S with enhancement extending down to 45°S . Maximum HCHO latitudes for ATom-3 and -4



268 (spring/fall) are near the equator ($\pm 5^\circ$). For ATom-3 and ATom-4, HCHO is systematically higher in the Northern
269 Hemisphere for comparable latitudes (e.g., 3×10^{15} molecules cm^{-2} at 50° N vs. 2×10^{15} molecules cm^{-2} at 50° S for ATom-
270 3). This, along with the asymmetric summer maxima, suggests that HCHO precursors (e.g., methane and other VOCs) are
271 more concentrated in the Northern Hemisphere and impact the distribution of HCHO over the remote ocean. Increased NO_x
272 and ozone can also promote formation of OH and thus HCHO.



273
274 **Figure 2. HCHO column density from three satellite retrievals (OMI SAO in red, OMPS SAO in blue, and OMI BIRA in orange)**
275 **and ATom in situ measurements (black) at different latitudes. The dots represent the averaged column density for $\pm 5^\circ$ latitude**
276 **bins and the bars are the standard deviation within the latitude bin. OMI SAO error bars are vertically offset for clarity.**

277
278 Continental outflows enhance HCHO near the coast, varying with seasons (Figure 1). Enhancements near East Asia, South
279 Asia, North America and Europe are highest during boreal summertime (ATom-1) and lowest during boreal winter time
280 (ATom-2), reflecting higher biogenic emissions and stronger photochemistry during the former. Biomass burning outflow
281 from Africa also varied with seasons, peaking during ATom-2 north of the equator and ATom-1 south of the equator. The
282 biomass burning outflows from Africa impacted the ATom-2, -3 and -4 flights and thus the Atlantic transits have higher
283 HCHO concentrations than Pacific transits. The biomass burning impacted air masses are not excluded in the analysis
284 because the African biomass burning outflows affect large areas and likely happen yearly and can be considered as part of
285 the background.

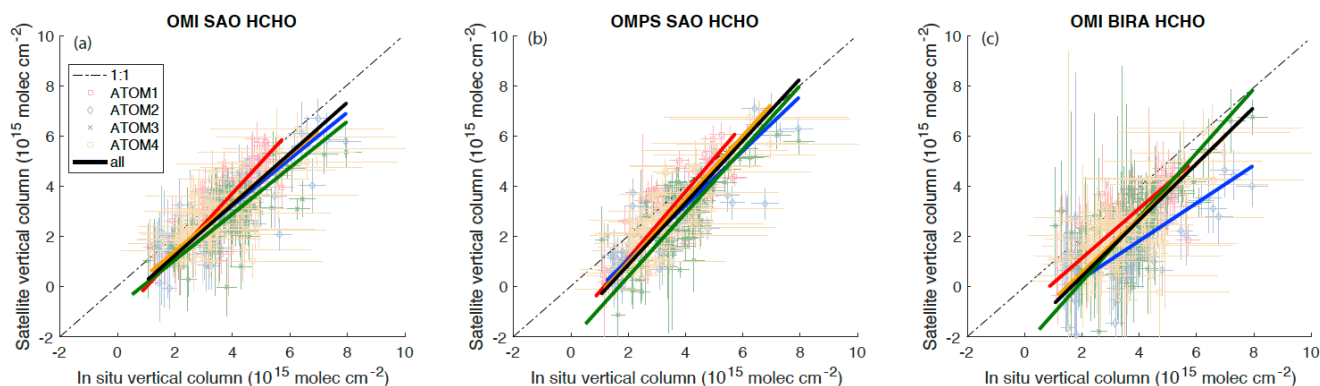
286 3.2 Comparison between retrievals and in situ HCHO columns

287 Comparison of satellite HCHO with ATom in situ composite column densities provides validation of satellite HCHO over
288 remote oceans, assuming ATom sampling is representative of the monthly average conditions. All retrievals (OMI SAO,
289 OMPS SAO and OMI BIRA) are well correlated with in situ integrated columns ($r^2 \geq 0.74$), with slopes ranging from 0.75
290 to 1.33 for individual seasons and negative intercepts on the order of 1×10^{15} molecules cm^{-2} (Figure 3; Table 2). The
291 uncertainty in HCHO above 10 km is on the order of 10^{14} molecules cm^{-2} and cannot account for the negative intercepts.
292 Persistent negative intercepts may suggest a low bias or offset in all retrievals, maybe related to modeled HCHO. GEOS-
293 Chem predicted HCHO was higher than observed during TRACE-P (Singh et al., 2004) and in-between two HCHO
294 observations during INTEX-A (Millet et al., 2006). Considering all retrievals, OMI SAO exhibits the best agreement with
295 ATom overall (slope = 1.02 ± 0.05 , intercept = $-0.8 \pm 0.2 \times 10^{15}$ molecules cm^{-2}). Considering individual ATom
296 deployments, retrievals fall closest to the 1:1 line against ATom columns for ATom1 (Figure 3). For ATom-2, OMI BIRA



297 also appears to be systematically low with a slope of 0.75 ± 0.09 . Low OMI BIRA HCHO in ATom-2 is also evident in
 298 Figure 2.

299



300

301 **Figure 3. Scattered plots of satellite HCHO vertical columns from OMI SAO (a), OMPS SAO (b), and OMI BIRA (c) retrievals**
 302 **versus in situ integrated vertical columns from four seasons: ATom-1 (red), ATom-2 (blue), ATom-3 (green) and ATom-4**
 303 **(orange). Error bars for satellite data are the standard deviation of the averaged grid cells, while error bars for in situ composite**
 304 **columns are propagated from the uncertainty of the in situ measurements: $\pm 10\% + 10$ pptv (or $\sim 4.8 \times 10^{14}$ molec cm^{-2}) for ISAF**
 305 **and $\pm 40\%$ (or 40 pptv, whichever is greater) (or $\sim 1.9 \times 10^{15}$ molecules cm^{-2}) for TOGA. The colored lines and black line are the**
 306 **equally weighted linear regression for each ATom and the total ATom data, respectively. The 1: 1 line is shown as the dashed line.**
 307 **The slopes and intercepts are summarized in Table 2. The higher standard deviations of OMI BIRA HCHO data are due to some**
 308 **large negative values not filtered and do not imply large variation of OMI BIRA HCHO data.**

309

310 Table 2 Parameters for linear fits of satellite retrievals against ATom observations (see Figure 3).

	OMI SAO			OMPS SAO			OMI BIRA		
	Slope	Intercept ($\times 10^{15}$)	r^2	Slope	Intercept ($\times 10^{15}$)	r^2	Slope	Intercept ($\times 10^{15}$)	r^2
ATom-1	1.24 ± 0.11	-1.26 ± 0.41	0.84 ± 0.06	1.33 ± 0.10	-1.54 ± 0.39	0.85 ± 0.06	0.99 ± 0.12	-0.86 ± 0.45	0.77 ± 0.10
ATom-2	0.93 ± 0.07	-0.49 ± 0.27	0.85 ± 0.07	1.09 ± 0.07	-1.11 ± 0.24	0.89 ± 0.06	0.75 ± 0.09	-1.20 ± 0.31	0.78 ± 0.09
ATom-3	0.92 ± 0.08	-0.79 ± 0.33	0.81 ± 0.08	1.27 ± 0.10	-2.14 ± 0.39	0.83 ± 0.07	1.28 ± 0.14	-2.37 ± 0.54	0.77 ± 0.09
ATom-4	0.96 ± 0.11	-0.53 ± 0.38	0.79 ± 0.10	1.26 ± 0.10	-1.56 ± 0.34	0.85 ± 0.07	1.09 ± 0.16	-1.61 ± 0.55	0.74 ± 0.11
all	1.02 ± 0.05	-0.79 ± 0.18	0.58 ± 0.04	1.24 ± 0.05	-1.61 ± 0.18	0.66 ± 0.03	1.12 ± 0.07	-1.84 ± 0.27	0.42 ± 0.04

311

312 The agreement between satellite HCHO retrievals and in situ composite columns is latitude-dependent (Figure 2). Generally,
 313 negative bias is smaller near the equator and more pronounced at higher latitudes, although this depends on season (Figure
 314 2). This is probably indicative of issues with latitude-dependent background corrections in satellite retrievals and/or global
 315 model bias. A more holistic investigation of relevant models with other ATom observations (e.g., ozone, OH, CO, and other
 316 trace gases) may help diagnose the latter. Reactive bromine chemistry at high latitudes may also play a role in the latitude-
 317 dependent satellite retrieval bias as bromine oxide (BrO) is a potential interfering absorber at pptv levels with high
 318 uncertainty in its concentration distribution. Although the difference between in situ composite columns and satellite
 319 retrievals are larger toward high latitudes, in situ composite columns are higher than satellite retrievals even near the equator
 320 during ATom-3 (Figure 2). Satellite OMI SAO and OMPS SAO HCHO vertical columns are closer to OMI BIRA during
 321 ATom-3 than other seasons (Figure 2).



3.3 Differences between retrievals

The three satellite HCHO retrievals all captured the patterns of the enhanced continental outflows though there are some small differences among them. Due to the sensor signal to noise ratio and pixel resolution, OMPS SAO HCHO maps are smoother (less noisy) than OMI HCHO data. OMPS SAO HCHO tends to have higher values near continental outflow regions and lower values far away from the outflow regions than OMI SAO HCHO (Figure 1). Although most of the continental outflows are not captured by the ATom flight tracks that were usually over the remote oceans far away from the continents, OMPS SAO HCHO columns along the ATom flight tracks are still higher than OMI SAO at high values and lower than OMI SAO at lower values (Figure 3). OMI BIRA HCHO columns usually have lower values than the other two retrievals, especially for ATom2.

3.4 Factors contributing to retrieval differences

Here we compare each component of satellite retrievals that could contribute to the retrieval differences. First, OMI SAO and OMI BIRA HCHO data are compared to probe the impact of different algorithms on retrievals from the same sensor. Second, OMI SAO and OMPS SAO data are examined to investigate the impact of different sensors on the data with the same retrieval algorithm.

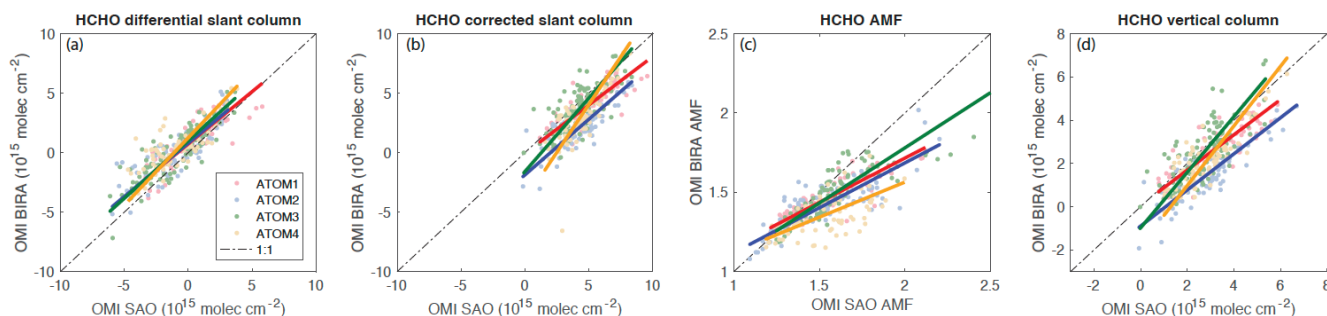


Figure 4 Comparison of the (a) HCHO differential slant column, (b) corrected slant column, (c) AMF, and (d) vertical column between OMI BIRA and OMI SAO for each ATom deployment.

Table 3 Parameters for linear fits of OMI BIRA vs OMI SAO retrievals subsampled over ATom flights tracks (see Figure 4).

	OMI BIRA vs OMI SAO											
	Differential slant column			Corrected slant column			AMF			Vertical column		
	Slope	Intercept ($\times 10^{15}$)	r^2	Slope	Intercept ($\times 10^{15}$)	r^2	Slope	Intercept	r^2	Slope	Intercept	r^2
ATom-1	0.88±0.06	0.73±0.12	0.72±0.05	0.81±0.07	-0.06±0.37	0.66±0.07	0.55±0.03	0.60±0.05	0.79±0.06	0.82±0.06	0.06±0.22	0.70±0.06
ATom-2	0.90±0.07	0.80±0.14	0.70±0.05	0.94±0.08	-1.87±0.36	0.63±0.08	0.58±0.05	0.55±0.07	0.64±0.07	0.84±0.06	-0.90±0.18	0.71±0.06
ATom-3	0.97±0.06	1.00±0.13	0.74±0.04	1.23±0.13	-1.59±0.58	0.47±0.07	0.69±0.38	0.39±0.06	0.76±0.05	1.28±0.11	-0.98±0.33	0.56±0.05
ATom-4	1.13±0.14	1.25±0.22	0.45±0.12	1.61±0.16	-3.99±0.68	0.57±0.11	0.44±0.06	0.68±0.10	0.37±0.07	1.38±0.13	-1.79±0.39	0.57±0.13

341



342 3.4.1 OMI SAO vs OMI BIRA

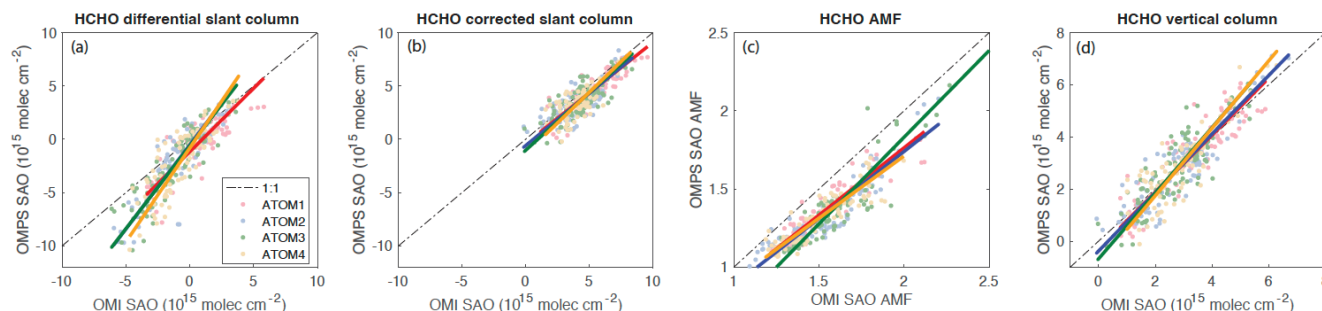
343 Differential HCHO slant column densities of OMI BIRA and OMI SAO are generally well correlated with slopes of 0.8 –
344 1.1 and intercepts of about 1×10^{15} molecules cm^{-2} (Figure 4a, Table 3). Because slant column values are the differential
345 between measured spectra over ocean and the reference sector spectrum, the slant column values go both positive and
346 negative. Differences in differential slant columns may be due to both the retrieval wavelength range and the reference
347 spectrum (Table 1). The strong O_4 absorption at 356.5–359 nm may contribute to the higher differential HCHO slant column
348 in OMI BIRA than OMI SAO; Nowlan et al. (2023) shows that the difference between the two fitting windows is typically
349 $< 4 \times 10^{14}$ molecules cm^{-2} at clean background levels. HCHO absorption cross sections used in the two retrievals come from
350 different sources (see Table 1). The different chosen reference spectra may also contribute to the difference between OMI
351 BIRA and OMI SAO slant columns. The OMI SAO reference spectrum at each across-track position is the average of
352 spectra between 30°N to 30°S in the orbit with closest in time and an equator crossing closest to 160°W and within
353 140° – 180°W (Nowlan et al., 2023). The OMI BIRA reference spectrum is using the daily average spectrum from the day
354 before for each across-track row in equatorial pacific region (latitude 5°N to 5°S and longitude 120° – 180°W) (De Smedt et
355 al., 2018).

356
357 Conversion to corrected slant columns generally reduces agreement between the two retrievals (Figure 4b). Background
358 HCHO slant columns at slightly different reference sectors and potential other corrections from different models are added
359 so the corrected slant columns are shifted to mostly positive values. The variability in slopes in the two retrievals among
360 different ATom seasons is larger in corrected slant column than in differential slant column, which may be caused by the
361 differences in background HCHO concentrations from different models results. The background HCHO and corrections for
362 OMI SAO and OMPS SAO are from a GEOS-Chem 2018 monthly climatology (Nowlan et al., 2023), while the background
363 HCHO and corrections for OMI BIRA is from the TM5-MP model daily data (De Smedt et al., 2021, 2017).

364
365 Despite the relatively large differences in AMFs, agreement between retrievals for corrected slant columns and vertical
366 columns is relatively similar (Figure 4d). Slopes are similar, and correlation coefficients actually improve by 5-10% with the
367 vertical columns. Partly this is because the range of variability in AMFs is small (factor of 2) compared to variability in
368 corrected slant columns (factor of 10). This implies that systematic uncertainties in AMFs are likely minor contributors to
369 overall retrieval error in remote environments.



370 **3.4.2 OMI SAO vs OMPS SAO**



371
 372 **Figure 5. Comparison of the (a) HCHO differential slant column, (b) corrected slant column, (c) AMF, and (d) vertical column**
 373 **between OMPS SAO and OMI SAO for each ATom deployment.**

374
 375 Table 4. Parameters for linear fits of OMPS SAO vs OMI SAO retrievals subsampled over ATom flights tracks (see Figure
 376 5).

	OMI SAO vs OMPS SAO											
	Differential slant column			Corrected slant column			AMF			Vertical column		
	Slope	Intercept ($\times 10^{15}$)	r^2	Slope	Intercept ($\times 10^{15}$)	r^2	Slope	Intercept	r^2	Slope	Intercept	r^2
ATom-1	1.19±0.10	-1.17±0.18	0.65±0.06	0.95±0.07	-0.41±0.35	0.74±0.05	0.86±0.04	0.04±0.06	0.85±0.02	1.09±0.07	-0.31±0.25	0.77±0.04
ATom-2	1.58±0.10	-0.52±0.20	0.77±0.06	0.98±0.08	-0.60±0.37	0.63±0.07	0.86±0.04	0.03±0.06	0.84±0.03	1.12±0.06	-0.38±0.19	0.80±0.05
ATom-3	1.55±0.08	-0.62±0.17	0.81±0.02	1.08±0.09	-1.04±0.39	0.61±0.06	1.11±0.04	-0.39±0.07	0.86±0.04	1.26±0.08	-0.68±0.23	0.72±0.05
ATom-4	1.76±0.13	-0.82±0.23	0.69±0.05	1.15±0.10	-1.37±0.45	0.61±0.08	0.80±0.05	0.12±0.07	0.80±0.03	1.30±0.08	-0.85±0.24	0.77±0.05

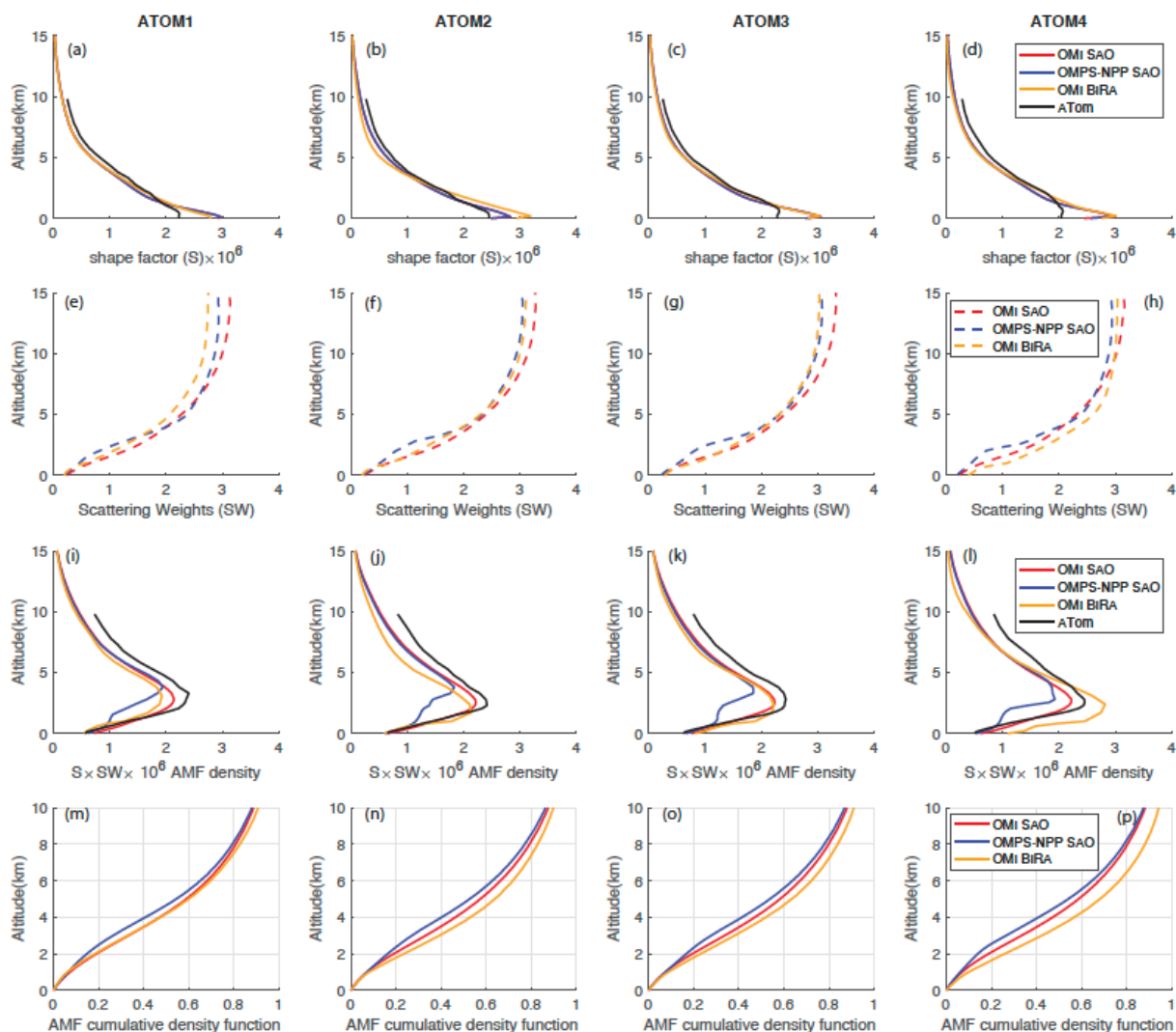
377
 378 Differential slant columns from OMI SAO and OMPS SAO are generally well correlated ($r^2 = 0.65-0.81$), with OMPS SAO
 379 slant columns lower at low values (Figure 5a). Different sensor properties and calibrations for the two sensors are likely
 380 explanations for these differences. Correction for cross-track pixel dependence sensitivity, HCHO background slant column,
 381 and latitude-dependent biases greatly improves agreement, with slopes near 1 for corrected slant columns (Figure 5b).

382
 383 The AMF of OMPS SAO is usually lower than OMI SAO (Figure 5c). Because the *a priori* gas profiles and scattering
 384 weights for OMPS SAO and OMI SAO with the same retrieval algorithms are from the same models, their AMF difference
 385 could be due to the different pixel size and the related cloud product, with OMPS SAO using climatology cloud pressure
 386 (Nowlan et al., 2023) in scattering weight calculation. The low OMPS SAO to OMI SAO AMF ratios brought the ratios of
 387 their vertical columns slightly higher than the ratios of their corrected slant columns. The correlation between OMPS SAO
 388 and OMI SAO is improved after normalization by AMF to yield vertical columns, which is similar to the comparison of
 389 OMI SAO and OMI BIRA, but the slopes get slightly further from 1.

390
 391 Although uncertainties in AMFs are likely minor contributors to overall retrieval error in remote ocean environments, roles
 392 of *a priori* profiles and scattering weights in contributing to the differences in AMF among the three retrievals are explored.
 393 Shape factors (S), scattering weights (SW), AMF density ($S \times SW \times 10^6$), and AMF accumulative density function for season
 394 average are shown in Figure 6. To better visualize the profiles, shape factors only below 15 km are shown in Figure 6,
 395 although ATom shape factors are available in altitudes up to ~10 km and satellite shape factors are up to 40 km. The



396 average shape factors of OMI SAO and OMPS SAO are identical due to the same chemical transport model outputs GEOS-
397 Chem 2018 monthly climatology $0.5^\circ \times 0.5^\circ$ data used. OMI BIRA shape factors are close to SAO shape factors except for
398 ATom-2, where OMI BIRA has higher HCHO values near the surface. To be noted, OMI BIRA HCHO is significantly
399 lower than the other two retrievals during ATom-2 (Figure 2). ATom shape factors tend to have lower distribution near the
400 surface than satellite shape factors. OMI SAO and OMPS SAO scattering weights come from the same radiative transfer
401 model VLIDORT v2.8 while scattering weights of OMI BIRA come from VLIDORT v2.7. However, OMPS SAO uses a
402 different cloud product for the scattering weights calculation. The climatology cloud data OMPS SAO uses are fixed at the
403 same height all the time for a given location, giving OMPS SAO the characteristic bump feature near 2 km and leading to the
404 difference in AMF density distribution with OMI SAO and OMI BIRA having one peak along altitude axis at ~ 3 km and
405 OMPS SAO having a peak at higher altitude (~ 4 km). AMF density distribution profiles using ATom *a priori* profiles show
406 similar maximum altitudes to the OMI satellite data. Due to the order of calculations, AMFs estimated from average *a priori*
407 and scattering weight of OMI BIRA are not always smaller than that of OMI SAO as shown in Figure 4c. Three satellite
408 retrievals all show that about 10% of AMF density distribution is above 10 km, which was not measured by ATom
409 observations.



410
 411
 412
 413
 414
 415
 416

Figure 6. Air mass factor (AMF) components shape factor (S) (a-d), scattering weights (SW) (e-h), and the product of S and SW ($S \times SW$) defined as AMF density (i-l) and the AMF cumulative density function (m-p) for the three satellite retrievals (red: OMI-SAO, blue: OMPS-NPP SAO, orange: OMI BIRA, black: derived from ATom measurements) and four seasons (different columns). ATom shape factor S comes from ATom in situ profiles.

417 4. Conclusions

418 We use in situ HCHO measurements from four seasonal deployments of the NASA ATom airborne mission to evaluate three
 419 satellite retrievals (OMI-SAO (v004), OMPS-NPP SAO, and OMI-BIRA) of total HCHO columns. All retrievals correlate
 420 with in situ composite columns over the remote marine regions, with OMI-SAO retrieval exhibiting the best agreement.
 421 Retrievals also capture the patterns of zonal gradients and seasonal variability, with the best agreement near the equator and



422 persistent negative bias at higher latitudes. OMI BIRA HCHO is consistently lower than the other two retrievals, with
423 anomalously low HCHO in February 2017. The discovery of latitude-dependent biases provides useful information for future
424 improvement of satellite HCHO retrievals.

425
426 Intercomparison of results from intermediate retrieval steps reveals the influence of different algorithms and different
427 sensors on derived HCHO columns. Notably, 1) OMI BIRA and SAO differences seem to be mainly due to the applied
428 background corrections, 2) OMI and OMPS have different differential SCDs but corrections fix most of that though OMPS
429 is still slightly higher at high values and lower at low values than OMI, and 3) AMFs can be significantly different, but they
430 don't seem to affect agreement between retrievals because the dynamic range of AMFs is relatively small.

431
432 Evaluation of retrievals using in situ composite columns implies that 1) retrievals of HCHO in remote regions do contain
433 actual measurement information, but models also affect retrieval accuracy; 2) retrievals may be sufficient as inputs to
434 parameterize OH or other species not directly measured from space, but the potential latitude-dependent systematic bias of
435 up to 2×10^{15} molecules cm^{-2} , which is substantial in the remote marine regions, should be considered; 3) this study
436 considered one species in a relatively simple region of the atmosphere, and retrieval differences will vary by molecule and
437 by location. Vertical profiles from in situ instruments are clearly crucial for providing ground truth needed to validate
438 satellite retrievals.

439 **Data availability**

440 The NASA ATom data are available at DAAC archive (<https://doi.org/10.3334/ORNDAAC/1925>). OMI SAO v004 data
441 are available at Harvard SAO server (https://waps.cfa.harvard.edu/sao_atmos/data/omi_hcho/). OMPS SAO data are
442 available at NASA GES DISC archive (<https://doi.org/10.5067/IIM1GHT07QA8>). The OMI BIRA data are available at
443 temis Website (<https://www.temis.nl/qa4ecv/hcho.html>; <https://doi.org/10.18758/71021031>).

444

445 **Author contributions**

446 GMW initiated and guided the project. AEK searched for the best satellite datasets to use, contacted satellite people to get
447 the satellite dataset, and used codes from JL to process some satellite data. JL wrote codes to grid and process the satellite
448 datasets and used codes from GMW to calculate in situ composite column. JL re-processed and analyzed the data and
449 discussed the results with GMW and JN. JL wrote the manuscript. GMW, JMISC, and TFH collected ATom ISAF data.
450 GGA, CRN, ZA and IDS provided satellite data. GGA provided the key equation to grid the satellite data. CRN provided



451 additional useful information for the satellite retrievals. ECA and RSH collected ATom TOGA data. All authors reviewed
452 and/or commented on the manuscript.

453 **Competing interests**

454 At least one of the (co-)authors is a member of the editorial board of Atmospheric Measurement Techniques.

455 **Acknowledgments**

456 JL, GMW, AEK, JN, JMSC, and TFH are supported by NASA Tropospheric Composition Program (TCP). JL, AEK, JN,
457 and JMSC are also supported by NOAA Atmospheric Chemistry, Carbon Cycle and Climate (AC4) program
458 (NA19OAR4310164). GGA, CRN and ZA are supported by NASA Making Earth System Data Records for Use in Research
459 Environments (80NSSC18M0091), algorithm maintenance for SAO standard OMI products (80NSSC21K0177), and
460 Algorithm maintenance for SAO OMI products (80NSSC24K0120). GGA and CRN are also supported by NASA Science of
461 Terra, Aqua, and Suomi-NPP (80NSSC18K0691). ECA and RSH are supported by the NSF National Center for
462 Atmospheric Research, which is a major facility sponsored by the U.S. National Science Foundation under Cooperative
463 Agreement No. 1852977.

464

465 **References**

- 466 Apel, E. C., Hills, A. J., Lueb, R., Zindel, S., Eisele, S., and Riemer, D. D.: A fast-GC/MS system to measure C₂ to C₄
467 carbonyls and methanol aboard aircraft, *Journal of Geophysical Research: Atmospheres*, 108, 2002JD003199,
468 <https://doi.org/10.1029/2002JD003199>, 2003.
- 469 Apel, E. C., Hornbrook, R. S., Hills, A. J., Blake, N. J., Barth, M. C., Weinheimer, A., Cantrell, C., Rutledge, S. A., Basarab,
470 B., Crawford, J., Diskin, G., Homeyer, C. R., Campos, T., Flocke, F., Fried, A., Blake, D. R., Brune, W., Pollack, I., Peischl,
471 J., Ryerson, T., Wennberg, P. O., Crouse, J. D., Wisthaler, A., Mikoviny, T., Huey, G., Heikes, B., O'Sullivan, D., and
472 Riemer, D. D.: Upper tropospheric ozone production from lightning NO_x-impacted convection: Smoke ingestion case
473 study from the DC3 campaign, *Journal of Geophysical Research: Atmospheres*, 120, 2505–2523,
474 <https://doi.org/10.1002/2014JD022121>, 2015.
- 475 Baublitz, C. B., Fiore, A. M., Ludwig, S. M., Nicely, J. M., Wolfe, G. M., Murray, L. T., Commane, R., Prather, M. J.,
476 Anderson, D. C., Correa, G., Duncan, B. N., Follette-Cook, M., Westervelt, D. M., Bourgeois, I., Brune, W. H., Bui, T. P.,
477 DiGangi, J. P., Diskin, G. S., Hall, S. R., McKain, K., Miller, D. O., Peischl, J., Thames, A. B., Thompson, C. R., Ullmann,
478 K., and Wofsy, S. C.: An observation-based, reduced-form model for oxidation in the remote marine troposphere, *Proc. Natl.
479 Acad. Sci. U.S.A.*, 120, e2209735120, <https://doi.org/10.1073/pnas.2209735120>, 2023.
- 480 Brune, W. H., Miller, D. O., Thames, A. B., Allen, H. M., Apel, E. C., Blake, D. R., Bui, T. P., Commane, R., Crouse, J.
481 D., Daube, B. C., Diskin, G. S., DiGangi, J. P., Elkins, J. W., Hall, S. R., Hanisco, T. F., Hannun, R. A., Hints, E. J.,
482 Hornbrook, R. S., Kim, M. J., McKain, K., Moore, F. L., Neuman, J. A., Nicely, J. M., Peischl, J., Ryerson, T. B., St. Clair,
483 J. M., Sweeney, C., Teng, A. P., Thompson, C., Ullmann, K., Veres, P. R., Wennberg, P. O., and Wolfe, G. M.: Exploring



- 484 Oxidation in the Remote Free Troposphere: Insights From Atmospheric Tomography (ATom), *Journal of Geophysical*
485 *Research: Atmospheres*, 125, e2019JD031685, <https://doi.org/10.1029/2019JD031685>, 2020.
- 486 Cazorla, M., Wolfe, G. M., Bailey, S. A., Swanson, A. K., Arkinson, H. L., and Hanisco, T. F.: A new airborne laser-induced
487 fluorescence instrument for in situ detection of formaldehyde throughout the troposphere and lower stratosphere, *Atmos.*
488 *Meas. Tech.*, 8, 541–552, <https://doi.org/10.5194/amt-8-541-2015>, 2015.
- 489 Chance, K.: Ultraviolet and visible spectroscopy and spaceborne remote sensing of the Earth’s atmosphere, *Comptes Rendus*
490 *Physique*, 6, 836–847, <https://doi.org/10.1016/j.crhy.2005.07.010>, 2005.
- 491 Chance, K. and Orphal, J.: Revised ultraviolet absorption cross sections of H₂CO for the HITRAN database, *Journal of*
492 *Quantitative Spectroscopy and Radiative Transfer*, 112, 1509–1510, <https://doi.org/10.1016/j.jqsrt.2011.02.002>, 2011.
- 493 Chance, K., Palmer, P. I., Spurr, R. J. D., Martin, R. V., Kurosu, T. P., and Jacob, D. J.: Satellite observations of
494 formaldehyde over North America from GOME, *Geophysical Research Letters*, 27, 3461–3464,
495 <https://doi.org/10.1029/2000GL011857>, 2000.
- 496 Chance, K., Liu, X., Miller, C. C., González Abad, G., Huang, G., Nowlan, C., Souri, A., Suleiman, R., Sun, K., Wang, H.,
497 Zhu, L., Zoogman, P., Al-Saadi, J., Antuña-Marrero, J.-C., Carr, J., Chatfield, R., Chin, M., Cohen, R., Edwards, D.,
498 Fishman, J., Flittner, D., Geddes, J., Grutter, M., Herman, J. R., Jacob, D. J., Janz, S., Joiner, J., Kim, J., Krotkov, N. A.,
499 Lefer, B., Martin, R. V., Mayol-Bracero, O. L., Naeger, A., Newchurch, M., Pfister, G. G., Pickering, K., Pierce, R. B.,
500 Rivera Cárdenas, C., Saiz-Lopez, A., Simpson, W., Spinei, E., Spurr, R. J. D., Szykman, J. J., Torres, O., and Wang, J.:
501 TEMPO Green Paper: Chemistry, physics, and meteorology experiments with the Tropospheric Emissions: monitoring of
502 pollution instrument, in: *Sensors, Systems, and Next-Generation Satellites XXIII*, *Sensors, Systems, and Next-Generation*
503 *Satellites XXIII*, Strasbourg, France, 10, <https://doi.org/10.1117/12.2534883>, 2019.
- 504 Chance, K. V., Spurr, R. J. D., Kurosu, T. P., Palmer, P. I., Martin, R. V., Fiore, A., Li, Q., and Jacob, D. J.: Tropospheric
505 formaldehyde measurements from the ESA GOME instrument, *Second International Asia-Pacific Symposium on Remote*
506 *Sensing of the Atmosphere, Environment, and Space*, Sendai, Japan, 1–9, <https://doi.org/10.1117/12.416945>, 2001.
- 507 De Smedt, I., Müller, J.-F., Stavrou, T., Van Der A, R., Eskes, H., and Van Roozendael, M.: Twelve years of global
508 observations of formaldehyde in the troposphere using GOME and SCIAMACHY sensors, *Atmos. Chem. Phys.*, 8, 4947–
509 4963, <https://doi.org/10.5194/acp-8-4947-2008>, 2008.
- 510 De Smedt, I., Van Roozendael, M., Stavrou, T., Müller, J.-F., Lerot, C., Theys, N., Valks, P., Hao, N., and Van Der A, R.:
511 Improved retrieval of global tropospheric formaldehyde columns from GOME-2/MetOp-A addressing noise reduction and
512 instrumental degradation issues, *Atmos. Meas. Tech.*, 5, 2933–2949, <https://doi.org/10.5194/amt-5-2933-2012>, 2012.
- 513 De Smedt, I., Stavrou, T., Hendrick, F., Danckaert, T., Vlemmix, T., Pinardi, G., Theys, N., Lerot, C., Gielen, C.,
514 Vigouroux, C., Hermans, C., Fayt, C., Veeffkind, P., Müller, J.-F., and Van Roozendael, M.: Diurnal, seasonal and long-term
515 variations of global formaldehyde columns inferred from combined OMI and GOME-2 observations, *Atmos. Chem. Phys.*,
516 15, 12519–12545, <https://doi.org/10.5194/acp-15-12519-2015>, 2015.
- 517 De Smedt, I., van Geffen, J., Richter, A., Beirle, S., Yu, H., Vlietinck, J., Van Roozendael, M., van der A, R., Lorente, A.,
518 Scanlon, T., Compernelle, S., Wagner, T., Eskes, H., and Boersma, F.: *OMI QA4ECV Product User Guide for HCHO*
519 (Version 1.0), 2017.
- 520 De Smedt, I., Theys, N., Yu, H., Danckaert, T., Lerot, C., Compernelle, S., Van Roozendael, M., Richter, A., Hilboll, A.,
521 Peters, E., Pedergnana, M., Loyola, D., Beirle, S., Wagner, T., Eskes, H., Van Geffen, J., Boersma, K. F., and Veeffkind, P.:



- 522 Algorithm theoretical baseline for formaldehyde retrievals from S5P TROPOMI and from the QA4ECV project, *Atmos.*
523 *Meas. Tech.*, 11, 2395–2426, <https://doi.org/10.5194/amt-11-2395-2018>, 2018.
- 524 De Smedt, I., Pinardi, G., Vigouroux, C., Compernelle, S., Bais, A., Benavent, N., Boersma, F., Chan, K.-L., Donner, S.,
525 Eichmann, K.-U., Hedelt, P., Hendrick, F., Irie, H., Kumar, V., Lambert, J.-C., Langerock, B., Lerot, C., Liu, C., Loyola, D.,
526 Piters, A., Richter, A., Rivera Cárdenas, C., Romahn, F., Ryan, R. G., Sinha, V., Theys, N., Vlietinck, J., Wagner, T., Wang,
527 T., Yu, H., and Van Roozendael, M.: Comparative assessment of TROPOMI and OMI formaldehyde observations and
528 validation against MAX-DOAS network column measurements, *Atmos. Chem. Phys.*, 21, 12561–12593,
529 <https://doi.org/10.5194/acp-21-12561-2021>, 2021.
- 530 Fortems-Cheiney, A., Chevallier, F., Pison, I., Bousquet, P., Saunois, M., Szopa, S., Cressot, C., Kurosu, T. P., Chance, K.,
531 and Fried, A.: The formaldehyde budget as seen by a global-scale multi-constraint and multi-species inversion system,
532 *Atmos. Chem. Phys.*, 12, 6699–6721, <https://doi.org/10.5194/acp-12-6699-2012>, 2012.
- 533 Franco, B., Marais, E. A., Bovy, B., Bader, W., Lejeune, B., Roland, G., Servais, C., and Mahieu, E.: Diurnal cycle and
534 multi-decadal trend of formaldehyde in the remote atmosphere near 46° N, *Atmos. Chem. Phys.*, 16, 4171–4189,
535 <https://doi.org/10.5194/acp-16-4171-2016>, 2016.
- 536 Goldberg, D. L., Lamsal, L. N., Loughner, C. P., Swartz, W. H., Lu, Z., and Streets, D. G.: A high-resolution and
537 observationally constrained OMI NO₂ satellite retrieval, *Atmos. Chem. Phys.*, 17, 11403–11421,
538 <https://doi.org/10.5194/acp-17-11403-2017>, 2017.
- 539 González Abad, G., Liu, X., Chance, K., Wang, H., Kurosu, T. P., and Suleiman, R.: Updated Smithsonian Astrophysical
540 Observatory Ozone Monitoring Instrument (SAO OMI) formaldehyde retrieval, *Atmos. Meas. Tech.*, 8, 19–32,
541 <https://doi.org/10.5194/amt-8-19-2015>, 2015.
- 542 González Abad, G., Vasilkov, A., Seftor, C., Liu, X., and Chance, K.: Smithsonian Astrophysical Observatory Ozone
543 Mapping and Profiler Suite (SAO OMPS) formaldehyde retrieval, *Atmos. Meas. Tech.*, 9, 2797–2812,
544 <https://doi.org/10.5194/amt-9-2797-2016>, 2016.
- 545 Guenther, A., Hewitt, C. N., Erickson, D., Fall, R., Geron, C., Graedel, T., Harley, P., Klinger, L., Lerdau, M., McKay, W.
546 A., Pierce, T., Scholes, B., Steinbrecher, R., Tallamraju, R., Taylor, J., and Zimmerman, P.: A global model of natural
547 volatile organic compound emissions, *Journal of Geophysical Research: Atmospheres*, 100, 8873–8892,
548 <https://doi.org/10.1029/94JD02950>, 1995.
- 549 Gulde, S. T., Kolm, M. G., Maurer, R., Sallusti, M., Bagnasco, G., Smith, D. J., and Bazalgette Courrèges-Lacoste, G.:
550 Sentinel 4: a geostationary imaging UVN spectrometer for air quality monitoring: status of design, performance and
551 development, in: International Conference on Space Optics — ICSO 2014, International Conference on Space Optics 2014,
552 Tenerife, Canary Islands, Spain, 39, <https://doi.org/10.1117/12.2304099>, 2017.
- 553 Herman, J., Cede, A., Spinei, E., Mount, G., Tzortziou, M., and Abuhassan, N.: NO₂ column amounts from ground-based
554 Pandora and MFDOAS spectrometers using the direct-sun DOAS technique: Intercomparisons and application to OMI
555 validation, *Journal of Geophysical Research: Atmospheres*, 114, 2009JD011848, <https://doi.org/10.1029/2009JD011848>,
556 2009.
- 557 Kim, J., Jeong, U., Ahn, M.-H., Kim, J. H., Park, R. J., Lee, H., Song, C. H., Choi, Y.-S., Lee, K.-H., Yoo, J.-M., Jeong, M.-
558 J., Park, S. K., Lee, K.-M., Song, C.-K., Kim, S.-W., Kim, Y. J., Kim, S.-W., Kim, M., Go, S., Liu, X., Chance, K., Chan
559 Miller, C., Al-Saadi, J., Veihelmann, B., Bhartia, P. K., Torres, O., Abad, G. G., Haffner, D. P., Ko, D. H., Lee, S. H., Woo,
560 J.-H., Chong, H., Park, S. S., Nicks, D., Choi, W. J., Moon, K.-J., Cho, A., Yoon, J., Kim, S., Hong, H., Lee, K., Lee, H.,
561 Lee, S., Choi, M., Veeffkind, P., Levelt, P. F., Edwards, D. P., Kang, M., Eo, M., Bak, J., Baek, K., Kwon, H.-A., Yang, J.,



- 562 Park, J., Han, K. M., Kim, B.-R., Shin, H.-W., Choi, H., Lee, E., Chong, J., Cha, Y., Koo, J.-H., Irie, H., Hayashida, S.,
563 Kasai, Y., Kanaya, Y., Liu, C., Lin, J., Crawford, J. H., Carmichael, G. R., Newchurch, M. J., Lefer, B. L., Herman, J. R.,
564 Swap, R. J., Lau, A. K. H., Kurosu, T. P., Jaross, G., Ahlers, B., Dobber, M., McElroy, C. T., and Choi, Y.: New Era of Air
565 Quality Monitoring from Space: Geostationary Environment Monitoring Spectrometer (GEMS), *Bulletin of the American
566 Meteorological Society*, 101, E1–E22, <https://doi.org/10.1175/BAMS-D-18-0013.1>, 2020.
- 567 Kwon, H. -A., Abad, G. G., Nowlan, C. R., Chong, H., Souri, A. H., Vigouroux, C., Röhling, A., Kivi, R., Makarova, M.,
568 Notholt, J., Palm, M., Winkler, H., Té, Y., Sussmann, R., Rettinger, M., Mahieu, E., Strong, K., Lutsch, E., Yamanouchi, S.,
569 Nagahama, T., Hannigan, J. W., Zhou, M., Murata, I., Grutter, M., Stremme, W., De Mazière, M., Jones, N., Smale, D., and
570 Morino, I.: Validation of OMPS Suomi NPP and OMPS NOAA-20 Formaldehyde Total Columns With NDACC FTIR
571 Observations, *Earth and Space Science*, 10, e2022EA002778, <https://doi.org/10.1029/2022EA002778>, 2023.
- 572 Kwon, H.-A., Park, R. J., González Abad, G., Chance, K., Kurosu, T. P., Kim, J., De Smedt, I., Van Roozendael, M., Peters,
573 E., and Burrows, J.: Description of a formaldehyde retrieval algorithm for the Geostationary Environment Monitoring
574 Spectrometer (GEMS), *Atmos. Meas. Tech.*, 12, 3551–3571, <https://doi.org/10.5194/amt-12-3551-2019>, 2019.
- 575 Li, C., Joiner, J., Krotkov, N. A., and Dunlap, L.: A new method for global retrievals of HCHO total columns from the
576 Suomi National Polar-orbiting Partnership Ozone Mapping and Profiler Suite, *Geophysical Research Letters*, 42, 2515–
577 2522, <https://doi.org/10.1002/2015GL063204>, 2015.
- 578 Millet, D. B., Jacob, D. J., Turquety, S., Hudman, R. C., Wu, S., Fried, A., Walega, J., Heikes, B. G., Blake, D. R., Singh, H.
579 B., Anderson, B. E., and Clarke, A. D.: Formaldehyde distribution over North America: Implications for satellite retrievals
580 of formaldehyde columns and isoprene emission, *Journal of Geophysical Research: Atmospheres*, 111, 2005JD006853,
581 <https://doi.org/10.1029/2005JD006853>, 2006.
- 582 Novak, G. A. and Bertram, T. H.: Reactive VOC Production from Photochemical and Heterogeneous Reactions Occurring at
583 the Air–Ocean Interface, *Acc. Chem. Res.*, 53, 1014–1023, <https://doi.org/10.1021/acs.accounts.0c00095>, 2020.
- 584 Nowlan, C. and Gonzalez Abad, G.: README Document for OMPS_NPP_NMHCHO_L2 and
585 OMPS_N20_NMHCHO_L2, 2022.
- 586 Nowlan, C. R., González Abad, G., Kwon, H., Ayazpour, Z., Chan Miller, C., Chance, K., Chong, H., Liu, X., O’Sullivan,
587 E., Wang, H., Zhu, L., De Smedt, I., Jaross, G., Seftor, C., and Sun, K.: Global Formaldehyde Products From the Ozone
588 Mapping and Profiler Suite (OMPS) Nadir Mappers on Suomi NPP and NOAA-20, *Earth and Space Science*, 10,
589 e2022EA002643, <https://doi.org/10.1029/2022EA002643>, 2023.
- 590 Prather, M. J., Zhu, X., Flynn, C. M., Strode, S. A., Rodriguez, J. M., Steenrod, S. D., Liu, J., Lamarque, J.-F., Fiore, A. M.,
591 Horowitz, L. W., Mao, J., Murray, L. T., Shindell, D. T., and Wofsy, S. C.: Global atmospheric chemistry – which air
592 matters, *Atmos. Chem. Phys.*, 17, 9081–9102, <https://doi.org/10.5194/acp-17-9081-2017>, 2017.
- 593 Singh, H. B., Salas, L. J., Chatfield, R. B., Czech, E., Fried, A., Walega, J., Evans, M. J., Field, B. D., Jacob, D. J., Blake, D.,
594 Heikes, B., Talbot, R., Sachse, G., Crawford, J. H., Avery, M. A., Sandholm, S., and Fuelberg, H.: Analysis of the
595 atmospheric distribution, sources, and sinks of oxygenated volatile organic chemicals based on measurements over the
596 Pacific during TRACE-P, *Journal of Geophysical Research: Atmospheres*, 109, 2003JD003883,
597 <https://doi.org/10.1029/2003JD003883>, 2004.
- 598 Spurr, R. J. D.: VLIDORT: A linearized pseudo-spherical vector discrete ordinate radiative transfer code for forward model
599 and retrieval studies in multilayer multiple scattering media, *Journal of Quantitative Spectroscopy and Radiative Transfer*,
600 102, 316–342, <https://doi.org/10.1016/j.jqsrt.2006.05.005>, 2006.



- 601 Thomas, W., Hegels, E., Meisner, R., Slijkhuis, S., Spurr, R., and Chance, K.: Detection of trace species in the troposphere
602 using backscatter spectra obtained by the GOME spectrometer, in: IGARSS '98. Sensing and Managing the Environment.
603 1998 IEEE International Geoscience and Remote Sensing. Symposium Proceedings. (Cat. No.98CH36174), IGARSS '98.
604 Sensing and Managing the Environment. 1998 IEEE International Geoscience and Remote Sensing. Symposium
605 Proceedings. (Cat. No.98CH36174), Seattle, WA, USA, 2612–2614 vol.5, <https://doi.org/10.1109/IGARSS.1998.702295>,
606 1998.
- 607 Thompson, C. R., Wofsy, S. C., Prather, M. J., Newman, P. A., Hanisco, T. F., Ryerson, T. B., Fahey, D. W., Apel, E. C.,
608 Brock, C. A., Brune, W. H., Froyd, K., Katich, J. M., Nicely, J. M., Peischl, J., Ray, E., Veres, P. R., Wang, S., Allen, H. M.,
609 Asher, E., Bian, H., Blake, D., Bourgeois, I., Budney, J., Bui, T. P., Butler, A., Campuzano-Jost, P., Chang, C., Chin, M.,
610 Commane, R., Correa, G., Crouse, J. D., Daube, B., Dibb, J. E., DiGangi, J. P., Diskin, G. S., Dollner, M., Elkins, J. W.,
611 Fiore, A. M., Flynn, C. M., Guo, H., Hall, S. R., Hannun, R. A., Hills, A., Hints, E. J., Hodzic, A., Hornbrook, R. S., Huey,
612 L. G., Jimenez, J. L., Keeling, R. F., Kim, M. J., Kupc, A., Lacey, F., Lait, L. R., Lamarque, J.-F., Liu, J., McKain, K.,
613 Meinardi, S., Miller, D. O., Montzka, S. A., Moore, F. L., Morgan, E. J., Murphy, D. M., Murray, L. T., Nault, B. A.,
614 Neuman, J. A., Nguyen, L., Gonzalez, Y., Rollins, A., Rosenlof, K., Sargent, M., Schill, G., Schwarz, J. P., Clair, J. M. St.,
615 Steenrod, S. D., Stephens, B. B., Strahan, S. E., Strode, S. A., Sweeney, C., Thames, A. B., Ullmann, K., Wagner, N.,
616 Weber, R., Weinzierl, B., Wennberg, P. O., Williamson, C. J., Wolfe, G. M., and Zeng, L.: The NASA Atmospheric
617 Tomography (ATom) Mission: Imaging the Chemistry of the Global Atmosphere, *Bulletin of the American Meteorological*
618 *Society*, 103, E761–E790, <https://doi.org/10.1175/BAMS-D-20-0315.1>, 2022.
- 619 Vigouroux, C., Bauer Aquino, C. A., Bauwens, M., Becker, C., Blumenstock, T., De Mazière, M., García, O., Grutter, M.,
620 Guarin, C., Hannigan, J., Hase, F., Jones, N., Kivi, R., Koshelev, D., Langerock, B., Lutsch, E., Makarova, M., Metzger, J.-
621 M., Müller, J.-F., Notholt, J., Ortega, I., Palm, M., Paton-Walsh, C., Poberovskii, A., Rettinger, M., Robinson, J., Smale, D.,
622 Stavrakou, T., Stremme, W., Strong, K., Sussmann, R., Té, Y., and Toon, G.: NDACC harmonized formaldehyde time series
623 from 21 FTIR stations covering a wide range of column abundances, *Atmos. Meas. Tech.*, 11, 5049–5073,
624 <https://doi.org/10.5194/amt-11-5049-2018>, 2018.
- 625 Vigouroux, C., Langerock, B., Bauer Aquino, C. A., Blumenstock, T., Cheng, Z., De Mazière, M., De Smedt, I., Grutter, M.,
626 Hannigan, J. W., Jones, N., Kivi, R., Loyola, D., Lutsch, E., Mahieu, E., Makarova, M., Metzger, J.-M., Morino, I., Murata,
627 I., Nagahama, T., Notholt, J., Ortega, I., Palm, M., Pinardi, G., Röhling, A., Smale, D., Stremme, W., Strong, K., Sussmann,
628 R., Té, Y., Van Roozendaal, M., Wang, P., and Winkler, H.: TROPOMI–Sentinel-5 Precursor formaldehyde validation using
629 an extensive network of ground-based Fourier-transform infrared stations, *Atmos. Meas. Tech.*, 13, 3751–3767,
630 <https://doi.org/10.5194/amt-13-3751-2020>, 2020.
- 631 Wang, Y., Beirle, S., Lampel, J., Koukouli, M., De Smedt, I., Theys, N., Li, A., Wu, D., Xie, P., Liu, C., Van Roozendaal,
632 M., Stavrakou, T., Müller, J.-F., and Wagner, T.: Validation of OMI, GOME-2A and GOME-2B tropospheric
633 NO₂, SO₂ and HCHO products using MAX-DOAS observations from
634 2011 to 2014 in Wuxi, China: investigation of the effects of priori profiles and aerosols on the satellite products, *Atmos.*
635 *Chem. Phys.*, 17, 5007–5033, <https://doi.org/10.5194/acp-17-5007-2017>, 2017.
- 636 Wolfe, G. M., Nicely, J. M., St. Clair, J. M., Hanisco, T. F., Liao, J., Oman, L. D., Brune, W. B., Miller, D., Thames, A.,
637 González Abad, G., Ryerson, T. B., Thompson, C. R., Peischl, J., McKain, K., Sweeney, C., Wennberg, P. O., Kim, M.,
638 Crouse, J. D., Hall, S. R., Ullmann, K., Diskin, G., Bui, P., Chang, C., and Dean-Day, J.: Mapping hydroxyl variability
639 throughout the global remote troposphere via synthesis of airborne and satellite formaldehyde observations, *Proc. Natl.*
640 *Acad. Sci. U.S.A.*, 116, 11171–11180, <https://doi.org/10.1073/pnas.1821661116>, 2019.
- 641 Zara, M., Boersma, K. F., De Smedt, I., Richter, A., Peters, E., Van Geffen, J. H. G. M., Beirle, S., Wagner, T., Van
642 Roozendaal, M., Marchenko, S., Lamsal, L. N., and Eskes, H. J.: Improved slant column density retrieval of nitrogen dioxide
643 and formaldehyde for OMI and GOME-2A from QA4ECV: intercomparison, uncertainty characterisation, and trends,
644 *Atmos. Meas. Tech.*, 11, 4033–4058, <https://doi.org/10.5194/amt-11-4033-2018>, 2018.



645 Zhu, L., Jacob, D. J., Kim, P. S., Fisher, J. A., Yu, K., Travis, K. R., Mickley, L. J., Yantosca, R. M., Sulprizio, M. P., De
646 Smedt, I., Gonzalez Abad, G., Chance, K., Li, C., Ferrare, R., Fried, A., Hair, J. W., Hanisco, T. F., Richter, D., Scarino, A.
647 J., Walega, J., Weibring, P., and Wolfe, G. M.: Observing atmospheric formaldehyde (HCHO) from space: validation and
648 intercomparison of six retrievals from four satellites (OMI, GOME2A, GOME2B, OMPS) with
649 SEAC<sup>4</sup>RS aircraft observations over the Southeast US, Gases/Remote
650 Sensing/Troposphere/Chemistry (chemical composition and reactions), <https://doi.org/10.5194/acp-2016-162>, 2016.

651 Zhu, L., González Abad, G., Nowlan, C. R., Chan Miller, C., Chance, K., Apel, E. C., DiGangi, J. P., Fried, A., Hanisco, T.
652 F., Hornbrook, R. S., Hu, L., Kaiser, J., Keutsch, F. N., Permar, W., St. Clair, J. M., and Wolfe, G. M.: Validation of satellite
653 formaldehyde (HCHO) retrievals using observations from 12 aircraft campaigns, *Atmos. Chem. Phys.*, 20, 12329–12345,
654 <https://doi.org/10.5194/acp-20-12329-2020>, 2020.

655
656
657
658
659
660
661
662
663
664
665
666
667
668
669